

# Computational and AI-Assisted Design of Dual-Metal Single-Atom Catalyst for Oxygen Reduction Reaction

Evan Xie<sup>1</sup> and Xijun Wang<sup>\*,2</sup>

<sup>1</sup>Deerfield Academy, 7 Boyden Ln, Deerfield, MA 01342 USA

<sup>2</sup>Northwestern University, 2145 Sheridan Road, Evanston, IL 60208 USA

\*Email: [xijun@northwestern.edu](mailto:xijun@northwestern.edu)

**Keywords:** single-atom catalyst, oxygen reduction reaction, density functional theory, machine learning, catalysis

## Abstract

The electrocatalytic oxygen reduction reaction (ORR) plays a crucial role in numerous energy and sustainability systems, such as fuel cells, metal-air batteries, and water electrolyzers. It holds significant potential for renewable energy generation, transportation, and storage, heralding a cleaner and more sustainable future. Recent trends have shown increased use of single-atom catalysts (SACs), particularly metal-N<sub>4</sub> moieties grown on graphene-based 2D materials, for enhancing ORR efficiency. However, the rational design of SAC for high-performance ORR faces challenges due to unclear structure-property relationships and the limits of conventional experimental trial-and-error approaches. In this study, we harnessed the power of the density functional theory (DFT) calculations, combined with cutting-edge machine learning (ML) techniques, to explore 144 SACs featuring dual interacting M<sub>1</sub>-N<sub>4</sub> and M<sub>2</sub>-N<sub>4</sub> moieties (M<sub>1</sub>, M<sub>2</sub> = Mn, Fe, Co, Ni, Cu, Ru, Rh, Pd, Ag, Ir, Pt, Au), denoted as M<sub>1</sub>-M<sub>2</sub>, grown on graphene. Of all the catalysts we examined, Fe-Pd emerged as the top performer, achieving an impressive overpotential of 0.980 V in alkaline conditions — outperforming most previously reported SACs. Even more striking, 25 of the evaluated SACs surpassed the renowned Fe-N<sub>4</sub> SAC in catalytic efficiency, including more economically viable alternatives like Fe-Ag. Venturing further, we developed three ML models that accurately predict the overpotentials of various M<sub>1</sub>-M<sub>2</sub> SACs, showing their strong ability to capture the relationship between single-atom metal site properties and overpotential. These models provide useful navigation toolkits for the rational design of effective electrocatalysts. Our study sheds light on the path toward achieving efficient SAC-catalyzed ORR, contributing to a more sustainable and energy-efficient future.

Oxygen Reduction Reaction (ORR) is a fundamental electrochemical process that plays a crucial role in numerous energy conversion systems and technologies. It involves the reduction of oxygen molecules to form water or other oxygen-containing species.<sup>1</sup> The significance of ORR lies in its direct connection to critical applications, particularly in fuel cells and metal-air batteries, which are considered promising alternatives to conventional combustion-based power sources due to their environmental benefits and higher energy efficiency.<sup>1-4</sup> For example, in the galvanic battery reaction (**Figure 1a**), ORR occurs at the cathode, where oxygen reacts with electrons and protons to produce water (**Figure 1b**). This reaction is crucial for generating electricity in fuel cells, which have the potential to power various transportation modes and provide clean energy for industrial and residential sectors. Similarly, in metal-air batteries,<sup>5</sup> ORR takes place during the discharge phase, where oxygen is reduced to form metal oxides and release electrical energy.

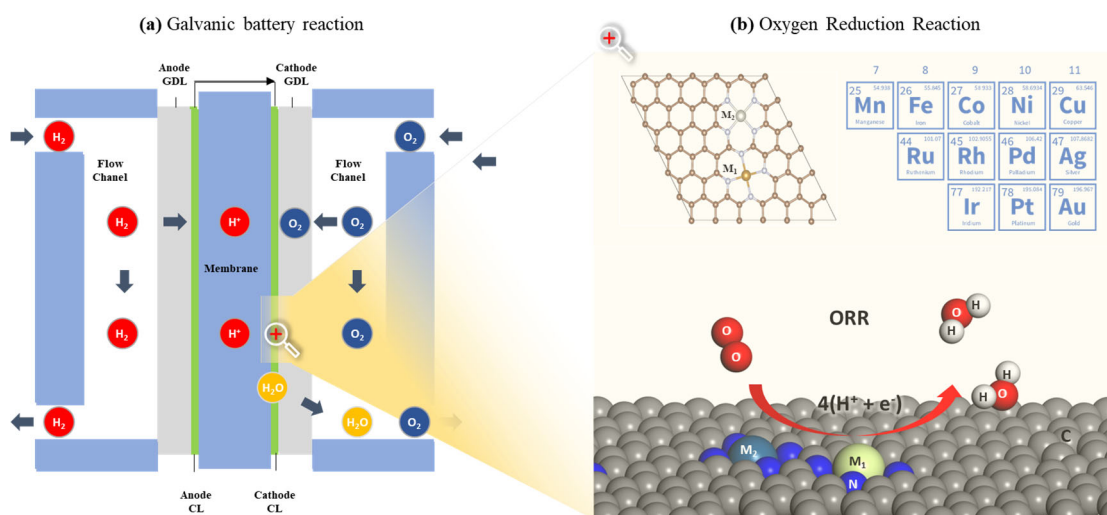


**Figure 1.** Schematic illustration of (a) the galvanic battery reaction and (b) ORR on  $M_1$ - $M_2$  SACs.

Efficient ORR is paramount for improving the overall performance and longevity of these energy conversion systems. However, the challenge lies in finding cost-effective catalysts that can enhance the kinetics of the ORR process and reduce energy losses. Researchers and engineers continue to explore new materials and design strategies to enhance ORR efficiency. To date, various materials and catalysts have been utilized in this area, including Pt-based electrocatalysts,<sup>6</sup> carbon nanotubes,<sup>7</sup> and transition metals alloys.<sup>8</sup> Among many types of materials, single-atom catalysts (SACs) stand out because of their minimal metal usage, superior efficiency, and enhanced selectivity.<sup>9-11</sup> Recently, Chen, Ji, *et al.* suggested a metal-organic framework (MOF) supported Fe

SAC,<sup>12</sup> which demonstrated excellent stability and catalytic performance with a positive half-wave potential of 0.912 V vs. Reversible Hydrogen Electrode (RHE). Liu *et al.* designed carbon-supported Pt SACs to improve the durability and efficiency of Pt SACs, achieving a positive half-wave potential of 0.87 vs RHE.<sup>13</sup> Rao *et al.* used novel “plasma bombing” strategies to design cheap Co single site SACs for enhanced ORR kinetics, with a Tafel slope of 79 mV dec<sup>-1</sup>.<sup>14</sup> These pioneering studies highlighted the efficacy and potential of SACs in enhancing ORR.

While researchers have made considerable progress in the development of SACs, the rational design of high-performance SACs for ORR remains a challenging task, primarily due to the limited understanding of the complex structure-property relationships governing their catalytic activity, especially at the atomic level.<sup>15</sup> Conventional experimental trial-and-error approaches often suffer from inefficiency and high costs. The iterative nature of this method necessitates a large number of time-consuming experiments and extensive materials testing, resulting in significant resource expenditure. Moreover, without a thorough comprehension of the underlying mechanisms, the outcomes of these experiments may lack consistency and fail to reach their full potential.

To address these challenges and accelerate SAC design, quantum chemistry methods, especially at the first-principles density functional theory (DFT) level,<sup>16, 17</sup> have been increasingly applied as powerful toolkits to enable a more systematic approach to predict and understand the catalytic behaviors of catalysts.<sup>18, 19</sup> These techniques empower researchers to explore a wide range of potential catalyst configurations and identify promising candidates for experimental synthesis, reducing the number of trial-and-error experiments and streamlining the design process. For example, Deng *et al.* adopted DFT to develop Co-based SACs on defective boron nitride (Co/BN) for efficient ORR.<sup>20</sup> Similarly, Yang *et al.* employed DFT to quantify the performance of two-dimensional conjugated aromatic networks (CAN) with a high single-metal-atom-site density that surpassed the performance of a conventional ORR catalyst, Pt/C SAC.<sup>21</sup> Further, Han *et al.* conducted DFT calculations to explore the ORR reaction mechanism and to evaluate the impact of the modulation effect on the ORR performance of Fe-N<sub>4</sub>/Pt-N<sub>4</sub> SACs.<sup>22</sup>

In recent years, there has been a notable surge in the utilization of cutting-edge machine learning (ML) techniques for materials design.<sup>23-25</sup> By training predictive models on data from theoretical simulations, researchers have rapidly and accurately screened promising catalytic materials for various applications, including ORR.<sup>26, 27</sup> This innovative approach has substantially

minimized the requirement for time-consuming DFT calculations and tedious experimental trial-and-error processes. Furthermore, the integration of DFT and ML offers in-depth insights into the intricate structure-property relationships governing catalyst activity, providing essential guidance for the rational design of SACs. This thereby accelerates the development of efficient and sustainable SACs for enhanced ORR, propelling the progress of clean energy technologies and addressing pressing environmental challenges.

In this study, using DFT and ML, we exhaustively investigated the ORR activity of 144 SACs with two M-N<sub>4</sub> moieties, denoted as M<sub>1</sub>-M<sub>2</sub>, where M<sub>1</sub> and M<sub>2</sub> = Mn, Fe, Ni, Co, Cu, Ru, Rh, Pd, Ag, Ir, Pt, Au (**Figure 1b**). These late transition metals were selected due to their promising potential in catalytic applications, especially ORR.<sup>28-31</sup> For each of the 144 SACs, we assessed their ORR performances by determining their overpotentials, which refers to the extra voltage necessary beyond the theoretical potential to drive the ORR at a desired rate. Through extensive overpotential calculations under alkaline conditions (pH = 13), we discovered twenty-five highly active SACs that exhibit superior performance compared to pristine Fe-N<sub>4</sub> SACs, previously regarded as active catalysts for ORR. Notably, we identified the Fe-Pd system as the most active SAC among all those investigated. Its overpotential (0.980 V) is even slightly lower than that of the previously discovered Fe-Pt SAC.<sup>22</sup> Furthermore, we found economical alternatives such as Fe-Ag, which exhibit comparable ORR activity with an overpotential of 1.008 V but at a significantly reduced cost. More intriguingly, we harnessed multiple ML methods to investigate the correlation between the intrinsic properties of the single-atom sites and their corresponding overpotentials. These ML models demonstrated high predictive power in estimating the overpotential, thereby effectively predicting promising SAC materials for ORR. These findings illuminate the ORR capabilities of various SAC materials, greatly broadening our understanding of material design and providing theoretical guidance for the future design and optimization of SAC materials, holding implications that transcend the realm of ORR.

This study primarily focuses on the 4-electron pathway, the most prevalent and desired pathway for ORR. This pathway directly produces water, avoiding the production of intermediate hydrogen peroxide seen in the 2-electron pathway. The overpotential was obtained using the analytical model developed by Nørskov<sup>32</sup> (see details in Section S1.1 in Supporting Information). The DFT calculations were performed using the Vienna ab initio Simulation package (VASP) (see details in

**Figure S1–S2**, and Section S1.2–1.4),<sup>33</sup> with the Perdew-Burke-Ernzerhof (PBE)<sup>34</sup> exchange-correlation functional and the all-electron projector augmented wave (PAW)<sup>35</sup> pseudopotential. To account for the strong on-site coulomb interactions for d-orbital electrons on the transition metal sites, the GGA+U approach<sup>36</sup> was applied, with The U values and initial spin state of each transition metal adopted from a previous benchmark study.<sup>37</sup>

Overpotential has been widely applied as a quantitative metric for assessing the performance of ORR, which is determined based on the binding free energies of the OOH\*, O\*, and OH\* intermediates. **Figure 2** summarizes the overpotentials of the 144 catalysts investigated in this work (refer to **Figure S3-S38** for the corresponding free energy profiles). While it is recognized that there is competition between M<sub>1</sub> and M<sub>2</sub> sites in binding the intermediates, for this simulation study that emphasizes the relationship between structure and properties, we assume that M<sub>1</sub> is the primary site responsible for intermediate binding. Given this premise, it's not surprising that the M<sub>1</sub> site can exert a more substantial influence on the overpotential of the system compared to M<sub>2</sub>. This is evidenced by the distinct patterns that emerged for specific M<sub>1</sub> metals. For example, the SACs with M<sub>1</sub> metals Ir, Rh, and Fe tend to exhibit lower overpotential values for most M<sub>2</sub> species, while catalysts involving Pd, Pt, and Ru generally show higher overpotentials. Nevertheless, we also show that the choice of M<sub>2</sub> is not insignificant – it can impact the catalytic behavior of M<sub>1</sub>. This is exemplified by the different performances of Fe-Mn and Fe-Pd. Fe-Mn presents a prohibitive overpotential of 1.985 V, denoting poor performance, whereas Fe-Pd demonstrates the lowest overpotential of 0.980 V, indicating superior performance. This observation underlines the importance of tuning the M<sub>1</sub>-M<sub>2</sub> composition for optimal ORR activity.

		M2												
		Mn	Fe	Ni	Co	Cu	Ru	Rh	Pd	Ag	Ir	Pt	Au	
M1	Mn	2.096	1.426	1.967	2.133	1.329	1.715	1.171	2.895	1.261	1.673	2.338	2.417	3
	Fe	1.985	1.259	1.234	1.501	1.276	1.310	1.331	0.980	1.008	1.353	0.983	1.520	2.8
	Ni	1.706	1.707	1.753	1.664	1.704	1.735	1.845	1.693	1.555	1.732	1.677	1.700	2.6
	Co	1.251	1.272	1.310	1.336	1.506	1.498	1.324	1.761	1.224	1.312	1.310	1.303	2.4
	Cu	1.748	1.686	1.707	1.487	1.743	1.746	1.504	1.737	1.740	1.704	2.007	1.554	2.2
	Ru	1.903	2.006	1.901	1.878	1.884	1.825	2.016	1.888	1.814	2.008	2.115	2.065	2
	Rh	1.010	1.038	1.030	1.506	1.273	1.100	1.137	1.044	1.099	1.126	1.029	1.238	1.8
	Pd	1.975	1.937	1.947	1.582	1.942	2.001	2.113	1.987	1.966	2.088	1.959	2.137	1.6
	Ag	1.416	1.678	1.585	1.543	1.153	1.283	1.385	1.145	1.175	1.287	1.584	1.444	1.4
	Ir	1.037	1.028	1.018	1.570	1.447	1.079	1.157	1.039	1.112	1.146	1.020	1.248	1.2
	Pt	1.981	1.991	1.990	1.961	1.996	1.939	2.157	2.006	2.255	2.148	2.039	1.935	1
	Au	1.705	1.665	1.602	1.648	2.096	1.834	2.132	2.073	1.907	1.852	2.098	1.237	0.8

**Figure 2.** Overpotential of the 144 SACs. Green values indicate low overpotential (high activity), Orange/Red values indicate high overpotential (low activity). Promising SACs with  $\eta < 1.18$  V are highlighted with red squares.

In our exhaustive study of the 144 M<sub>1</sub>-M<sub>2</sub> combinations, we have successfully pinpointed twenty-five SACs (highlighted with red squares in **Figure 2**) exhibiting lower overpotential than that of the benchmark catalyst, pristine Fe-N<sub>4</sub> (1.18 V).<sup>38</sup> This discovery is especially notable given the well-established efficacy of Fe-N<sub>4</sub> for ORR. Among the promising catalysts identified, Fe-Pt (with an overpotential of 0.983 V) and Fe-Pd (with an overpotential of 0.980 V) have been validated by previous experimental studies.<sup>22,39</sup>

This congruence between computational prediction and experimental validation not only bolsters the reliability of our computational methodology but also substantiates the promising potential of these catalyst candidates. Furthermore, our exploration unveiled four M<sub>1</sub>-M<sub>2</sub> combinations (Fe-Ag, Ag-Cu, Ag-Pd, Ag-Ag) that are not only close to the overpotential performance of Fe-Pd but are significantly less expensive. This crucial discovery opens the tantalizing possibility of achieving efficient ORR catalysis at a significantly reduced cost. These advancements could significantly accelerate the development and commercialization of cost-effective, high-performance ORR catalysts.

Next, we moved on to delve deeper into the determinants of overpotential, which hinges on the binding free energies of the OOH\*, O\*, and OH\* intermediates. Through a comprehensive

assessment of the  $\Delta G_{OOH^*}$ ,  $\Delta G_{OH^*}$ , and  $\Delta G_{O^*}$  binding free energies, we successfully delineated the scaling relationships between these quantities, as depicted in [1]-[3]:

$$\Delta G_{OOH^*} = 0.492657064 \times \Delta G_{O^*} + 1.106113111 \quad [1]$$

$$\Delta G_{OH^*} = 0.556863752 \times \Delta G_{O^*} - 0.352882071 \quad [2]$$

$$\Delta G_{OOH^*} = 0.826082575 \times \Delta G_{OH^*} + 1.445296836 \quad [3]$$

The strong linear relationships (**Figure 3a**, **Figure S39**) suggested that the binding energies of these intermediates on a given metal site tend to be intertwined, which presents a dilemma: a catalyst cannot simultaneously optimize the binding energy for all intermediates, leading to a trade-off where the optimization of the binding energy for one intermediate may result in a suboptimal binding energy for another intermediate. While overcoming this limitation is an ongoing research pursuit beyond the scope of this study, the discerned correlations offer a powerful analytical tool: they allow for the estimation of  $\Delta G_{OOH^*}$ ,  $\Delta G_{O^*}$ , and  $\Delta G_{OH^*}$  binding energies directly from each other, significantly streamlining the analysis of the interplay between binding energies and overpotential.

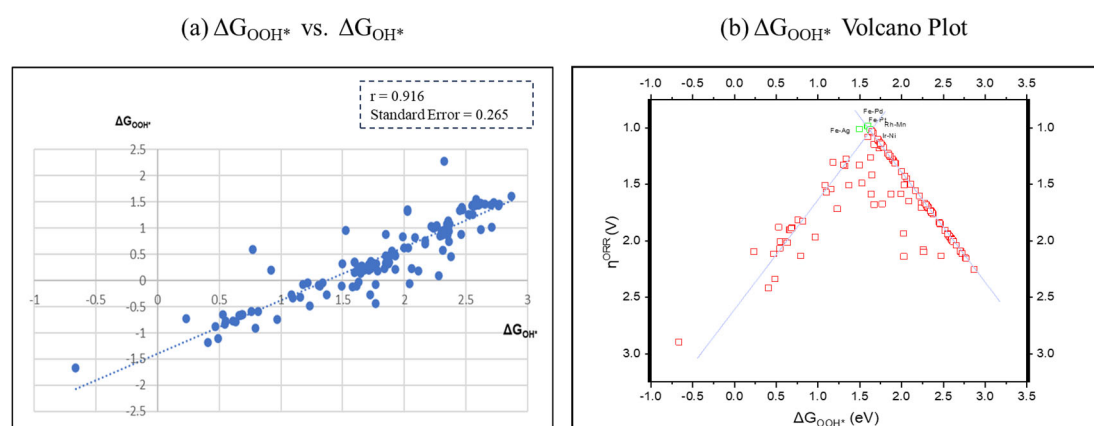


**Figure 3.** (a) Plot of the relationships between  $\Delta G_{OOH^*}$  and  $\Delta G_{OH^*}$  for the 144 SACs. (b) Overpotential as a function of  $\Delta G_{OOH^*}$  for the 144 SACs. The five best-performing  $M_1$ - $M_2$  SACs are highlighted in green and labeled. The apex of the volcano plot underscores the range of optimal binding energies for  $\Delta G_{OOH^*}$  (~1.59-1.78 eV).

Using one of the three binding free energies – in this case,  $\Delta G_{OOH^*}$  – as the x-axis and plotting the overpotential as the y-axis, we observed a distinctive volcano-shaped trend, also known as the Sabatier principle,<sup>40</sup> shown in **Figure 3b**. The peak of this volcano plot, ranging from approximately 1.59 – 1.78 eV, indicates an optimized region for catalytic activity based on catalysts whose overpotential is affected by  $\Delta G_{OOH^*}$  and has an overpotential  $\leq 1.18$  V. Catalysts falling within this optimal range of binding energies demonstrate enhanced activity for ORR, prominently displayed by the five best-performing catalysts: Fe-Pd ( $\eta = 0.980$  V), Fe-Pt ( $\eta = 0.986$  V), Fe-Ag ( $\eta = 1.008$



V), Rh-Mn ( $\eta = 1.010$  V), and Ir-Ni ( $\eta = 1.018$  V). The presence of perfect linear correlations on the right wing of the volcano shape in the  $\Delta G_{\text{OOH}^*}$  graph (**Figure 3b**) and on the left wing of the volcano shape in the  $\Delta G_{\text{OH}^*}$  graph (**Figure S40a**) signifies that the overpotential-determining step for ORR is primarily contributed either by the first step of  $^*\text{OOH}$  formation or the fourth step of  $^*\text{OH}$  desorption. These findings agree well with previous reports.<sup>41,42</sup> In comparison, the importance of  $\Delta G_{\text{O}^*}$  in determining the overpotential is relatively less, as demonstrated in the  $\Delta G_{\text{O}^*}$  volcano plot (**Figure S40b**).

Optimizing the  $\Delta G_{\text{OOH}^*}$  and/or  $\Delta G_{\text{OH}^*}$  values emerge as a compelling strategy to enhance ORR activity. This can be achieved through various strategies, including modifying the coordination environment surrounding the active metal site. For instance, the introduction of ligands, such as an OH group<sup>43</sup> near the active metal site, can alter its electronic structure. This could be achieved by the ligand either donating or withdrawing electrons from the metal center, thereby tuning the metal's electronic properties and enhancing its catalytic activity. Such modifications exert a direct influence on the strength and nature of the interactions between the metal and the adsorbate, thereby shaping the activity of the SACs. This emphasizes the critical significance of precise control over the electronic properties of catalysts, as it empowers the facilitation of efficient and targeted reactions.

Since binding energies play a crucial role in determining the overpotential, we presented them in the form of three distinct heat maps for  $\Delta G_{\text{OOH}^*}$  (**Figure 4**),  $\Delta G_{\text{OH}^*}$  (**Figure S41a**), and  $\Delta G_{\text{O}^*}$  (**Figure S41b**). Most of the Ir-M<sub>2</sub>, Fe-M<sub>2</sub>, and Rh-M<sub>2</sub> combinations exhibit optimal binding energies that are neither too strong nor too weak. These metal pairings enable sufficiently strong interactions to facilitate the reaction while avoiding overly strong binding that could impede the desorption of reaction intermediates. Conversely, the heat maps indicate that Ru-M<sub>2</sub> combinations generally display relatively weak binding energies with adsorbates. This suggests that the interaction between the Ru and the adsorbates may not be strong enough, which could potentially slow down reaction kinetics. On the other hand, the Pd-M<sub>2</sub>, Pt-M<sub>2</sub>, and Au-M<sub>2</sub> systems show exceedingly strong binding energies with adsorbates. Such intense interactions may hamper the release of adsorbed intermediates, which could result in decreased reactivity and sluggish reaction rates. These findings emphasize the delicate balancing act required in designing efficient SACs for ORR.

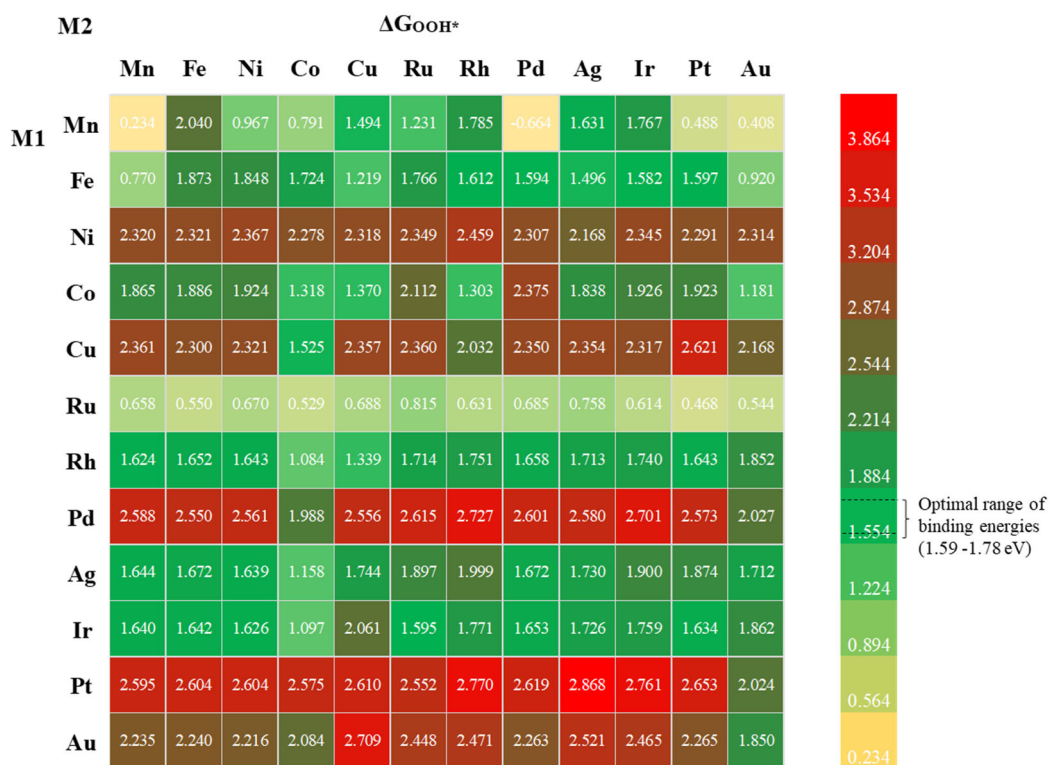


**Figure 4.**  $\Delta G_{\text{OOH}}^*$  for 144 SACs. Optimal binding energies ( $\sim 1.59$  -  $1.78$  eV) are represented in green, overly strong binding energies are marked in red, and excessively weak binding energies are denoted in yellow.

To understand how varying  $M_1$ - $M_2$  combinations result in different binding free energies, we directed our attention toward 12 systems with Fe as the  $M_1$  site (Fe- $M_2$ ). Previous work by Rosen *et al.*<sup>44</sup> suggested a strong correlation between the binding energies of a molecule on different metal sites and the group number of the metal elements, which is understandable given that the number of outermost electrons tends to increase as one moves across the periodic table. It is therefore reasonable to infer that an increase in  $M_2$ 's group number may subtly modify  $M_1$ 's behavior, leading to a gradual change in the binding affinity of intermediates on  $M_1$ . In light of this hypothesis, we plotted  $\Delta G_{\text{OOH}}^*$  against  $M_2$ 's group number (**Figure S42a**). Contrary to expectations, a careful examination of the data from group 7 to group 11 yielded a pattern resembling a volcano plot rather than a clear linear trend. The absence of a linear correlation suggests that different  $M_2$  elements interact uniquely with Fe, beyond simple electron donation or withdrawal mechanisms. Further complicating our understanding, no discernible pattern emerged when comparing the  $M_2$ 's group number with overpotential (**Figure S42b**). These observations prompt us to look beyond intrinsic properties and delve into the more complex interactions between the  $M_1$  and  $M_2$  sites. More in-depth analysis, such as molecular orbital hybridization analysis, might offer a more nuanced perspective

on the complex interactions between  $M_1$  and  $M_2$ , and, in turn, shed more light on how these interactions influence the binding of intermediates on  $M_1$  sites.

To further illuminate how binding free energies of the reaction intermediates can influence overpotential, we turned our focus to two extreme cases, Fe-Pd and Mn-Pd, which represent the best and worst-performing SACs, respectively. Their free energy profiles along the 4-electron pathway are shown in **Figure 5a** and **5b**. The Mn-Pd catalyst displays a significantly higher overpotential of 2.895 V compared to the Fe-Pd catalyst (0.980 V), demonstrating its inferior performance. Under  $U = 1.23$  V, it is apparent that energy increments at each step are more smoothly transitioned in the Fe-Pd catalyst compared to the Mn-Pd catalyst. For the latter, the energy steps on the three binding configurations are significantly more stable than the former, especially for the  $\text{OH}^*$  desorption step. In fact, Mn-Pd showcases the smallest  $\Delta G_{\text{OH}^*}$  value (-1.67 eV) amongst all the 144 systems studied, leading to a prohibitive barrier in the  $\text{OH}^*$  desorption step, leading to a notable decrease in its activity. Conversely, the Fe-Pd catalyst exhibits an optimal  $\Delta G_{\text{OH}^*}$  value (0.35 eV), corresponding to an enhanced ORR activity.

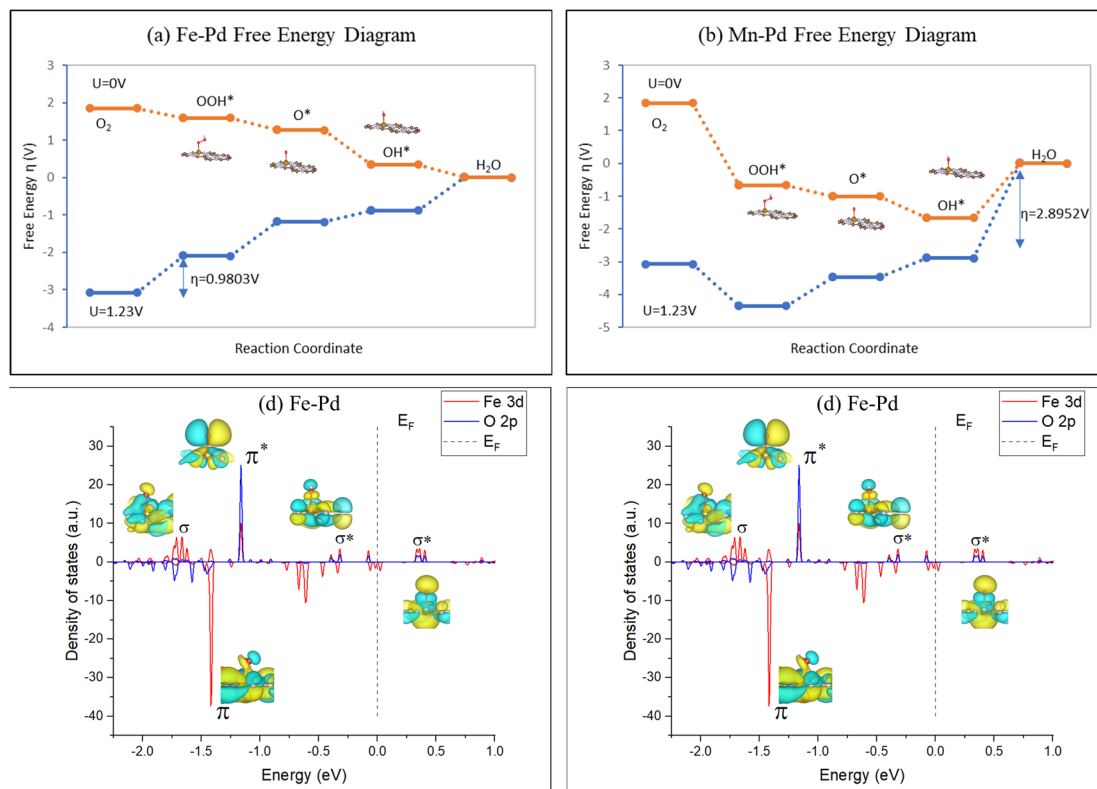


**Figure 5.** Comparison of the free energy profiles of (a) the best-performing SAC (Fe-Pd) and (b) the worst-performing SAC (Mn-Pd). Computed PDOS for (c) Fe-Pd and (d) Mn-Pd, after the binding of  $\text{OH}^*$  binding. The bonding molecular orbitals, denoted as  $\sigma$  and  $\pi$ , correspond to bonding interactions between the d-orbitals of Fe or

Mn and the p-orbitals of O.  $\sigma^*$  and  $\pi^*$  denote the antibonding molecular orbitals arising from interactions between the d orbitals of Fe or Mn and p orbitals of O.

To rationalize the huge difference in  $\Delta G_{\text{OH}^*}$  between Fe-Pd and Mn-Pd, we computed the projected density of states (PDOS) for the d-orbitals of  $M_1$  sites (Fe and Mn) and p-orbitals of O after  $\text{OH}^*$  binding in both systems. Specifically, we visualized the spatial distribution of molecular orbitals for the electronic states with high density or those close to the Fermi level ( $E_F$ ). These electronic states are depicted in **Figure 5c** and **5d**, as they are believed to play a critical role in determining the bonding strength of  $M_1\text{-OH}^*$ . In the case of  $\text{OH}^*$  binding on Fe-Pd (**Figure 5c**), the frontier orbitals for Fe-O bonding are primarily the  $\pi^*$  and  $\sigma^*$  antibonding orbitals, leading to relatively weak Fe-OH bonding. In contrast, the orbital energy levels and spatial distributions are remarkably different in the Mn-Pd system (**Figure 5d**). Near the Fermi level, we observed  $\sigma$  and  $\pi$  bonding orbitals, which considerably strengthen the Mn-O bonding. This leads to a significantly more negative  $\Delta G_{\text{OH}^*}$  value of -1.67 eV, which in turn results in a much higher overpotential of 2.895 V (**Figure 5c**). This detailed analysis of molecular orbital hybridization provides further insight into how different  $M_1\text{-}M_2$  combinations can dramatically affect the binding free energies and the overall ORR activity.

While molecular orbital analysis provides qualitative insights into the bonding strength between metal and intermediate reactants, quantitatively predicting overpotential from the readily available intrinsic atomic properties or easy-to-compute electronic properties of single-atom catalysts (SACs) remains a formidable task. This necessitates an in-depth, quantitative grasp of the structure-property relationship, a challenge intensified by the intricate interplay among, in our context,  $M_1\text{-}M_2$ , and  $M_1$ -intermediates. Although DFT is invaluable in analyzing these relationships, its usage is constrained by its time-consuming nature. Consequently, we turn to employing data-driven methodologies like machine learning (ML), as a potentially efficient and accurate alternative for overpotential prediction. As illustrated in **Figure 6a**, we considered 16 intrinsic or electronic features, including inherent properties such as electronegativity ( $\chi$ ), atomic radius ( $r_a$ ), atomic mass ( $m_a$ ), ionization energy ( $E_i$ ) of  $M_1$  and  $M_2$  metal atoms (denoted by subscripts  $_1$  and  $_2$ ), alongside DFT-derived electronic properties like spin-up and spin-down d-band centers ( $\epsilon_{d\uparrow}$  and  $\epsilon_{d\downarrow}$ ), partial charge ( $q$ ), spin density ( $\rho$ ) on  $M_1$  and  $M_2$ , and the HOMO-LUMO gap ( $E_g$ ) of the  $M_1\text{-}M_2$  systems. We employed two types of ML algorithms - Sure Independence Screening and Sparsity

Optimization (SISSO)<sup>45</sup> for feature space dimensional reduction (see details in Section S1.5), and the Extra Trees Regressor (ETR)<sup>46</sup>, a decision-tree-based regression approach (see details in Section S1.6). These algorithms were trained using 80% of the dataset comprising of 144 SACs and tested on the remaining 20% of the data.

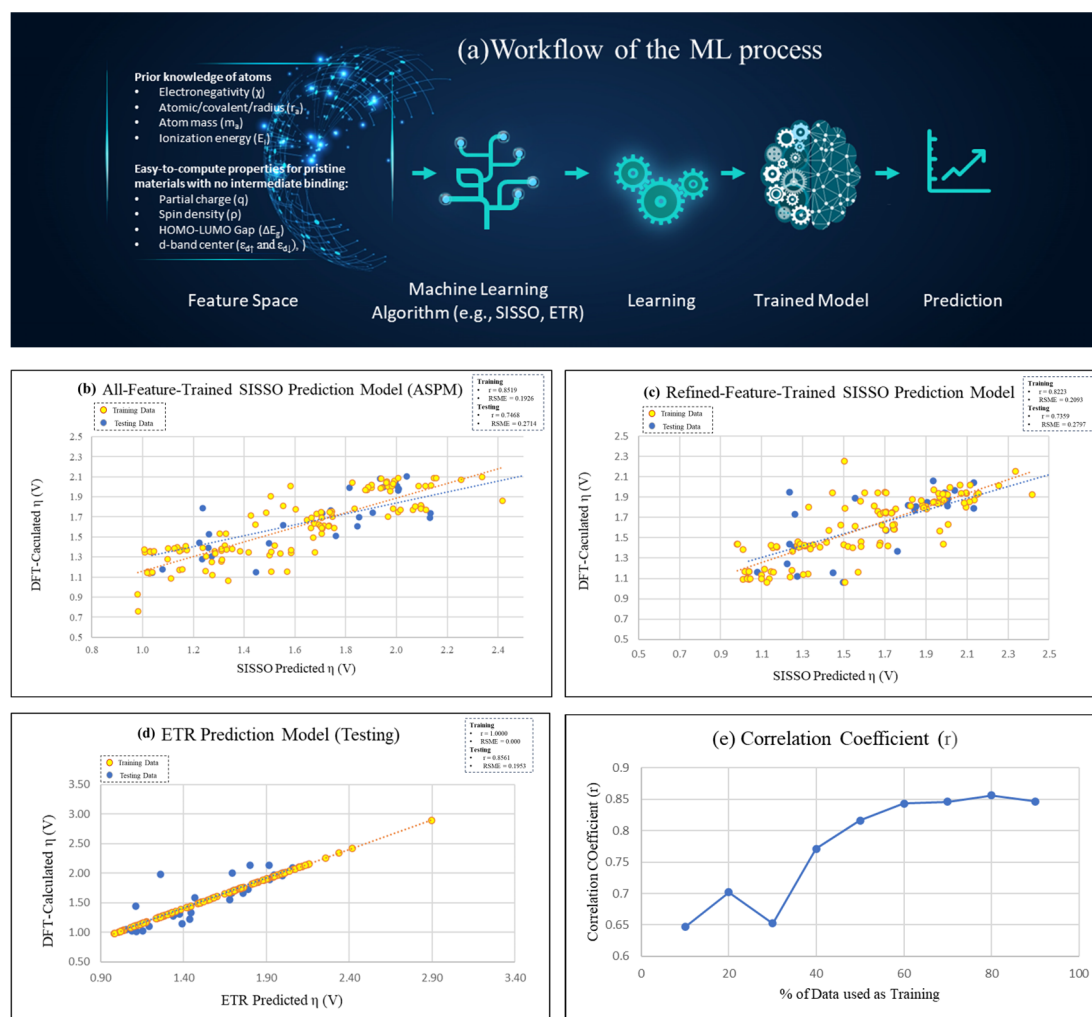


**Figure 6.** (a) Workflow of the ML process for predicting overpotential from intrinsic atomic properties and DFT-computed electronic properties. Prediction performance of the (b) ASPM SISSO, (c) RSPM SISSO, and (d) ETR models for the training (80%) and testing (20%) datasets. (e) Illustration of the incremental improvement in the predictive ability of the ETR model with increasing size of training datasets.

Firstly, we employed the SISSO method to bridge the input features – namely, the intrinsic atomic properties and DFT-computed electronic properties – and the target property (ORR overpotential). For this supervised learning task, SISSO constructed a feature space by mathematically combining each feature using a specified set of operators, represented as  $\hat{H} \equiv \{I, +, -, \times, \div, \log, \exp, \exp-, -1, 2, 3, 6, \sqrt{\cdot}, ||, \sin, \cos, \text{scd}\}$ .<sup>45</sup> Only physically meaningful combinations,

i.e., those with identical units, were retained. Sure-independence screening (SIS) was then used to rank and select descriptors based on their correlations with the target property. The sparsifying operator (SO) method was subsequently adopted to further promote descriptor space sparsity, effectively reducing the feature space dimensionality. This procedure generated a set of feature-operator combinations, which serve as descriptors for connecting features and overpotential.

The equation derived from these descriptors (eq. [4]) is as follows:

$$\eta_{\text{SISSO-Predicted}} = -0.365 \times \left[ \cos\left(\frac{m_{a1}}{\chi_1}\right) \right] - 1.408 \times |scd(E_{gl}) - \sin(q_1)| + 1.331 \times \left[ \frac{\chi_1 - \chi_2}{\left(\frac{\varepsilon_{d1}}{E_{gl}}\right)} \right] + 1.915 \quad [4]$$

This equation demonstrated statistically significant accuracy in predicting overpotential, with a significant correlation coefficient ( $r$ ) of 0.852 for the training datasets (**Figure 6b**). The Root Mean Square Error (RMSE) value of 0.193 V falls within the computational error of DFT, signifying a strong agreement between SISSO-predicted and DFT-computed values. When predicting for the testing datasets, the performance slightly deteriorated ( $r = 0.747$ ,  $\text{RMSE} = 0.271$  V, **Figure 6c**), hinting at possible overfitting. This may be attributed to including too many unrelated or interrelated features or a lack of sufficient datasets (in this instance, 144). Despite comprehensive attempts to improve the prediction accuracy of the SISSO model — such as incorporating more informative features (refer to Section S2.1 for more details), refining the selection of input features, and exploring alternative approaches to overpotential prediction (refer to Section S2.2 for more details) — we failed to achieve significant improvement. This outcome underscores the complexity of the problem and invites further investigation into novel predictive methodologies. Nevertheless, the results emphasize the relative precision of the descriptors generated by SISSO in capturing the quantitative relationship between features and overpotential.

More interestingly, upon closer inspection, eq. [4] is mainly comprised of  $M_1$  properties, which is expected since  $M_1$  is the site directly bonding with the reaction intermediates and should, therefore, govern the overpotential. The equation includes three key terms. The first term,  $\cos(\frac{m_{a1}}{\chi_1})$ , relates to  $M_1$ 's intrinsic properties, such as mass and electronegativity, which naturally influence the catalytic properties of the  $M_1$  site. The second term,  $scd(E_{gl}) - \sin(q_1)$ , represents the partial charge on the  $M_1$  site and the  $M_1$ - $M_2$  material's electronic bandgap, both crucial to catalytic activity. These parameters are influenced implicitly by the properties of  $M_2$ , hence indirectly incorporating  $M_2$ 's chemical information. The third term's numerator,  $\chi_1 - \chi_2$ , is the electronegativity difference between  $M_1$  and

M<sub>2</sub>, conveying the information of charge transfer between the metal sites, while the denominator,  $\frac{\epsilon_{d\downarrow}}{E_{g\downarrow}}$ , carries molecular orbital information. These terms validate our hypothesis that the catalytic properties of M<sub>1</sub>-M<sub>2</sub> are impacted by the interactions between the M<sub>1</sub>-N<sub>4</sub> and M<sub>2</sub>-N<sub>4</sub> sites. This happens even though the M<sub>1</sub>-N<sub>4</sub> and M<sub>2</sub>-N<sub>4</sub> sites are not directly connected, and extends beyond simple electron donation or withdrawal mechanisms. Importantly, these complex interactions can be quantified using the SISO-generated descriptors.

To mitigate the overfitting resulting from the small data problem, it is potentially beneficial to evaluate the relevance and significance of each feature. Less important features may introduce noise or bias, potentially leading to inaccurate predictions. Consequently, we refined the initial sixteen features used for training the model. The importance analysis for each feature was performed using the ETR algorithm, a commonly utilized decision tree-based ML method. This allowed us to assess the relative importance of each feature in determining the overpotential (**Table 1**). The refined features were selected based on a mean importance cutoff of 0.05, ensuring only the most informative and impactful features were retained. The refined feature set included the ionization energy of M<sub>1</sub> (E<sub>I1</sub>), d-band centers (ε<sub>d↑</sub> and ε<sub>d↓</sub>), spin density of M<sub>1</sub> (ρ<sub>1</sub>), partial charge of M<sub>1</sub> (q<sub>1</sub>), electronegativity of M<sub>1</sub> (χ<sub>1</sub>), and atomic radius of M<sub>1</sub> (r<sub>a1</sub>). Using these refined features, we formulated another SISO-generated equation as follows:

$$\eta_{\text{SISO-Predicted}} = 0.304 \times [\cos(\epsilon_{d\uparrow} + \epsilon_{d\downarrow})] - 0.363 \times \left[ \frac{\text{scd}(\epsilon_{d\uparrow})}{\cos(E_{I1})} \right] + 0.000575 \times \left[ \frac{\chi_1^6}{\sin(r_{a1})} \right] + 1.696 \quad [5]$$

**Table 1.** Evaluation of the mean importance for sixteen input features using the ETR Algorithm. Features with mean importance greater than 0.05 (bolded) were selected for the RSPM.

Features	Feature Mean Importance
<b>M<sub>1</sub>-Partial-charge (q<sub>1</sub>)</b>	0.300
<b>M<sub>1</sub>- Ionization (E<sub>I1</sub>)</b>	0.224
<b>M<sub>1</sub>- Electronegativity (χ<sub>1</sub>)</b>	0.125
<b>M<sub>1</sub>-Spin-density (ρ<sub>1</sub>)</b>	0.080
<b>Band-Up (ε<sub>d↑</sub>)</b>	0.062
<b>M<sub>1</sub>- Radius (r<sub>a1</sub>)</b>	0.061
<b>Band-Down (ε<sub>d↓</sub>)</b>	0.053

M <sub>1</sub> -Mass ( $m_{a1}$ )	0.038
Gap Down ( $E_{gl}$ )	0.016
M <sub>2</sub> -Electronegativity ( $\chi_2$ )	0.014
M <sub>2</sub> -Radius ( $r_{a2}$ )	0.012
M <sub>2</sub> -Ionization ( $E_{I2}$ )	0.011
M <sub>2</sub> -Mass ( $m_{a2}$ )	0.011
Gap Up ( $E_{g\uparrow}$ )	0.011
M <sub>2</sub> - Partial-charge ( $q_2$ )	0.006
M <sub>2</sub> -Spin-density ( $\rho_2$ )	0.002

The refined-feature-trained SISSO prediction model (RSPM) showed a correlation coefficient of  $r = 0.822$  and an RMSE value of 0.209 (**Figure 6c**). Although its performance is slightly lower than the model trained with ASPM, the RSPM provides a comparable outcome while requiring fewer computed features in the prediction equations, specifically the HOMO-LUMO gap and partial charge. For the testing set, the RSPM demonstrated a correlation coefficient ( $r$ ) of 0.736 and an RMSE value of 0.273 for the testing data (**Figure 6c**), close to the prediction performance of the ASPM model.

Subsequently, we utilized the ETR algorithm to predict overpotential based on the 16 features. A significant disparity was noted when comparing the performance of the ETR-based model on the training data (80%) and the testing data (20%). The model performed perfectly on the training data, showing an ideal correlation coefficient of  $r = 1.000$  and an RMSE value of 0.000 V (**Figure 6d**). However, its performance declined when applied to the testing data, producing a correlation coefficient of  $r = 0.856$  and an RMSE value of 0.195 V (**Figure 6d**). This divergence is reflective of overfitting, a classic challenge encountered with smaller datasets, where the model could excessively adapt to the training data at the expense of generalization. However, even with this noted dip in performance, our ETR model outperformed the SISSO model on the testing dataset, reinforcing the ETR's competitive edge in overpotential prediction. Most importantly, we see a clear path for the future advancement of our ETR model. We can, therefore, expect an improvement in the model prediction power with an increase in the size of the training datasets. **Figure 6e** depicts



that as the training dataset size grows, there's a marked increase in prediction accuracy. This suggests that expanding the training data could be a fruitful direction for the continued refinement and evolution of our model.

**Table 2** outlines the performance of the above-mentioned three ML models – the ASPM and RSPM SISSO models, and the ETR model. These models exhibit impressive performance, demonstrating the utility and effectiveness of ML in material design. Particularly, we applied these three models to predict promising  $M_1$ - $M_2$  combinations, using pristine Fe-N<sub>4</sub> ( $\eta = 1.18V$ ) as a benchmark. As detailed in **Table 3** and **Table 4**, the ASPM, RSPM SISSO models, and the ETR model predicted 17, 26, and 24 promising materials, respectively. DFT validations of these predictions highlighted 11, 17, and 24 successful matches, translating to success rates of 65%, 65%, and a stellar 100%, respectively.

In addition, we identified the top twenty-five catalysts via DFT calculations (highlighted with red squares in **Figure 2**), each surpassing the benchmark of pristine Fe-N<sub>4</sub>. We aimed to assess how many of these high-performing materials could be accurately predicted by our ML models. As detailed in **Table 4**, the results were fairly encouraging: the ASPM successfully predicted 44% (11 out of 25), while the RSPM identified a commendable 68% (17 out of 25), demonstrating the robust predictive capabilities of these models. In comparison to these SISSO models, the ETR model achieved a success rate of 96% (24 out of 25), although potential overfitting in the training dataset for the ETR model cannot be overlooked. However, its promising performance for the testing set still strongly supports its capacity for the rapid identification of high-potential materials.

These findings affirm that while ML models may not be flawless, they can significantly alleviate the burden of time-consuming DFT computations and expensive experimental procedures. The enhanced performance of the RSPM model in predicting top catalysts underscores the potential of refining such models to improve prediction accuracy, thus driving the field of materials science toward more efficient and precise discovery and development.

**Table 2.** ASPM (training and testing), RSPM (training and testing), and ETR (training and testing) model prediction statistics. Performance quantified by  $r$ ,  $r^2$ , RMSE, MAE.

Models	Coefficient ( $r$ )	$r^2$	RMSE	MAE
ASPM (Training)	0.852	0.726	0.193	0.558

<b>ASPM (Testing)</b>	0.747	0.558	0.271	0.994
<b>RSPM (Training)</b>	0.822	0.676	0.209	0.751
<b>RSPM (Testing)</b>	0.736	0.542	0.280	0.778
<b>ETR (Training)</b>	1.000	1.000	0.000	0.000
<b>ETR (Testing)</b>	0.856	0.733	0.195	0.724

**Table 3.** ASPM, RSPM, and ETR predictability of the top twenty-five DFT-computed catalysts. Red values indicate a false prediction of material. \* Indicates the testing result from ETR.

<b>M<sub>1</sub>-M<sub>2</sub></b>	<b>Overpotential</b>	<b>ASPM Predicted</b>	<b>RSPM Predicted</b>	<b>ETR Predicted</b>
Fe-Pd	0.980	0.927		0.980
Fe-Pt	0.983	0.758		0.983
Fe-Ag	1.008			1.008
Rh-Mn	1.010		1.091	1.116*
Ir-Ni	1.018		1.168	1.018
Ir-Pt	1.020	1.155	1.166	1.020
Ir-Fe	1.028	1.139	1.165	1.028
Rh-Pt	1.029		1.104	1.087*
Rh-Ni	1.030		1.095	1.155*
Ir-Mn	1.037	1.143	1.165	1.037
Rh-Fe	1.038		1.092	1.038
Ir-Pd	1.039	1.147	1.171	1.039
Rh-Pd	1.045		1.099	1.053*
Ir-Ru	1.079	1.177	1.161	1.079
Rh-Ag	1.099		1.133	1.192*
Rh-Ru	1.100		1.096	1.100
Ir-Ag	1.113	1.084		1.113
Rh-Ir	1.126		1.061	1.126
Rh-Rh	1.137		1.095	1.137
Ag-Pd	1.145			1.392*

Ir-Ir	1.146	1.172	1.166	1.146
Ag-Cu	1.153			1.153
Ir-Rh	1.157	1.179	1.164	1.157
Mn-Rh	1.171			1.171
Ag-Ag	1.175			1.175
Rh-Au	1.238		1.114	
Ir-Au	1.248	1.158	1.179	
Rh-Cu	1.273		1.121	
Fe-Cu	1.276	1.123		
Co-Au	1.303		1.141	
Co-Rh	1.325		1.145	
Co-Co	1.336	1.066		
Ir-Cu	1.448	1.148	1.154	
Co-Ru	1.498		1.06	
Rh-Co	1.505		1.064	
Co-Cu	1.506	1.153		
Ir-Co	1.57	1.153	1.162	

**Table 4.** Comparison of the performances of ASPM, RSPM, and ETR in predicting the top twenty-five DFT-computed catalysts.

	Total # of good catalysts predicted (A)	# of good catalysts confirmed by DFT (B)	% of good catalysts confirmed by DFT (C) = (B)/(A)	% of good predicted vs. 25 good catalysts by DFT (F) = (B)/25
ASPM	17	11	65%	44%
RSPM	26	17	65%	68%
ETR	24	24	100%	96%

In summary, we applied a synergistic approach of DFT calculations and ML techniques to explore the ORR performance of 144 SACs. We discovered 25 materials that outperformed the pristine Fe-N<sub>4</sub> benchmark, offering superior catalytic activity. Of particular interest, the Fe-Pd, Fe-Pt, and Fe-Ag catalysts emerged as top performers, delivering impressive overpotentials of 0.980

V, 0.983 V, and 1.008 V respectively, under alkaline conditions (pH = 13). This surpasses the performance of most, if not all, previously reported materials, and sets a promising precedent for the field. Especially noteworthy is the economic feasibility of Fe-Ag, given the abundant availability and cost-effectiveness of both iron (Fe) and silver (Ag). Additional catalysts, such as Ag-Cu, Ag-Pd, and Ag-Ag, showed promising performance alongside economic efficiency.

Our comprehensive analysis of adsorbate binding energies helped us pinpoint an optimal range for  $\Delta G_{\text{OOH}^*}$  (~1.59-1.78 eV) and  $\Delta G_{\text{OH}^*}$  (~0.15-0.37 eV). This range correlates with high catalytic performance, thereby providing valuable insight for future experimental optimization. Therefore, the potential to enhance overall catalyst performance through structural modifications that optimize active site binding energies is notable. To further delve into these insights, we conducted an orbital analysis on our best performing catalyst (Fe-Pd) and the least effective one (Mn-Pd). The analysis highlighted that the ideal binding strength of reaction intermediates arises from a balanced interaction between the bonding and anti-bonding orbitals in the frontier orbitals.

We trained ML models using a suite of atomic and electronic properties pertaining to the single-atom metal sites as input features to predict the overpotential of the SACs. Impressively, these models exhibited significant predictive prowess, with one of the SISSO models and the ETR model successfully reproducing 68% and 96% of the top-performing SACs, respectively. These results highlighted the potential of ML as a tool to reduce the need for costly DFT computations and to streamline experimental trial-and-error processes.

Collectively, our research lays a firm foundation for the intelligent design and discovery of SACs. We have not only illuminated the possibilities for a more sustainable and eco-friendly future but also set a foundation for further exploration of ORR performance and the application of ML in material design. This opens up the possibility for the development of highly efficient, cost-effective catalysts that could revolutionize energy conversion and storage applications, extending far beyond catalysis.

## References

1. Ge, X.; Sumboja, A.; Wu, D.; An, T.; Li, B.; Goh, F. W. T.; Hor, T. S. A.; Zong, Y.; Liu, Z. Oxygen Reduction in Alkaline Media: From Mechanisms to Recent Advances of Catalysts. *ACS Catal.* **2015**, *5* (8), 4643–4667.
2. Katsounaros, I.; Cherevko, S.; Zeradjanin, A. R.; Mayrhofer, K. J. J. Oxygen Electrochemistry as a Cornerstone for Sustainable Energy Conversion. *Angew. Chem., Int. Ed.* **2013**, *53* (1), 102–121.
3. Zaman, S.; Huang, L.; Abdoukader Ibro Douka; Yang, H.; You, B.; Bao Yu Xia. Oxygen Reduction Electrocatalysts toward Practical Fuel Cells: Progress and Perspectives. *Angew. Chem., Int. Ed.* **2021**, *60* (33), 17832–17852.
4. Liu, M.; Xiao, X.; Li, Q.; Luo, L.; Ding, M.; Zhang, B.; Li, Y.; Zou, J.; Jiang, B. Recent Progress of Electrocatalysts for Oxygen Reduction in Fuel Cells. *J. Colloid Interface Sci.* **2022**, *607*, 791–815.
5. Ma, R.; Lin, G.; Zhou, Y.; Liu, Q.; Zhang, T.; Shan, G.; Yang, M.; Wang, J. A Review of Oxygen Reduction Mechanisms for Metal-Free Carbon-Based Electrocatalysts. *Npj Comput. Mater.* **2019**, *5* (1).
6. Ma, Z.; Cano, Z. P.; Yu, A.; Chen, Z.; Jiang, G.; Fu, X.; Yang, L.; Wu, T.; Bai, Z.; Lu, J. Enhancing Oxygen Reduction Activity of Pt-Based Electrocatalysts: From Theoretical Mechanisms to Practical Methods. *Angew. Chem.* **2020**, *132* (42), 18490–18504.
7. Lu, Y.; Li, X.; Compton, R. G. Oxygen Reduction Reaction at Single Entity Multiwalled Carbon Nanotubes. *J. Phys. Chem. Lett.* **2022**, *13* (16), 3748–3753.
8. Wu, Z.-P.; Caracciolo, D. T.; Maswadeh, Y.; Wen, J.; Kong, Z.; Shan, S.; Vargas, J. A.; Yan, S.; Hopkins, E.; Park, K.; Sharma, A.; Ren, Y.; Petkov, V.; Wang, L.; Zhong, C.-J. Alloying–Realloying Enabled High Durability for Pt–Pd–3d-Transition Metal Nanoparticle Fuel Cell Catalysts. *Nat. Commun.* **2021**, *12* (1), 859.
9. Li, L.; Chang, X.; Lin, X.; Zhao, Z.-J.; Gong, J. Theoretical Insights into Single-Atom Catalysts. *Chem. Soc. Rev.* **2020**, *49* (22), 8156–8178.
10. Guo, J.; Liu, H.; Li, D.; Wang, J.; Djitchou, X.; He, D.; Zhang, Q. A Minireview on the Synthesis of Single Atom Catalysts. *RSC Adv.* **2022**, *12* (15), 9373–9394.

11. Wang, A.; Li, J.; Zhang, T. Heterogeneous Single-Atom Catalysis. *Nat. Rev. Chem.* **2018**, 2 (6), 65–81.
12. Chen, Y.; Ji, S.; Zhao, S.; Chen, W.; Dong, J.; Cheong, W.-C.; Shen, R.; Wen, X.; Zheng, L.; Rykov, A. I.; Cai, S.; Tang, H.; Zhuang, Z.; Chen, C.; Peng, Q.; Wang, D.; Li, Y. Enhanced Oxygen Reduction with Single-Atomic-Site Iron Catalysts for a Zinc-Air Battery and Hydrogen-Air Fuel Cell. *Nat. Commun.* **2018**, 9 (1).
13. Liu, J.; Jiao, M.; Lu, L.; Barkholtz, H. M.; Li, Y.; Wang, Y.; Jiang, L.; Wang, Y.; Liu, D.-J.; Zhuang, L.; Ma, C.; Zeng, J.; Zhang, B.; Dang Sheng Su; Zou, M.-H.; Xing, W.; Xu, W.; Jiang, Z.; Sun, G. High Performance Platinum Single Atom Electrocatalyst for Oxygen Reduction Reaction. *Nat. Commun.* **2017**, 8 (1).
14. Rao, P.; Wu, D.; Wang, T.-J.; Li, J.; Deng, P.; Chen, Q.; Shen, Y.; Chen, Y.; Tian, X. Single Atomic Cobalt Electrocatalyst for Efficient Oxygen Reduction Reaction. *eScience* **2022**, 2 (4), 399–404.
15. Li, J.; Chen, C.; Xu, L.; Zhang, Y.; Wei, W.; Zhao, E.; Wu, Y.; Chen, C. Challenges and Perspectives of Single-Atom-Based Catalysts for Electrochemical Reactions. *J. Am. Chem. Soc.* **2023**, 3 (3), 736–755.
16. Jain, A.; Shin, Y.; Persson, K. A. Computational Predictions of Energy Materials Using Density Functional Theory. *Nat. Rev. Mater.* **2016**, 1 (1), 1–13.
17. Fu, C.; Liu, C.; Li, T.; Zhang, X.; Wang, F.; Yang, J.; Jiang, Y.; Cui, P.; Li, H. DFT Calculations: A Powerful Tool for Better Understanding of Electrocatalytic Oxygen Reduction Reactions on Pt-Based Metallic Catalysts. *Comput. Mater. Sci.* **2019**, 170, 109202.
18. Makkar, P.; Ghosh, N. N. A Review on the Use of DFT for the Prediction of the Properties of Nanomaterials. *RSC Adv.* **2021**, 11 (45), 27897–27924.
19. Florian Kraushofer; Parkinson, G. S. Single-Atom Catalysis: Insights from Model Systems. *Chem. Rev.* **2022**, 122 (18), 14911–14939.
20. Deng, C.; He, R.; Shen, W.; Li, M.; Zhang, T. A Single-Atom Catalyst of Cobalt Supported on a Defective Two-Dimensional Boron Nitride Material as a Promising Electrocatalyst for the Oxygen Reduction Reaction: A DFT Study. *Phys. Chem. Chem. Phys.* **2019**, 21 (13), 6900–6907.

21. Yang, S.; Yu, Y.; Dou, M.; Zhang, Z.; Dai, L.; Wang, F. Two-Dimensional Conjugated Aromatic Networks as High-Site-Density and Single-Atom Electrocatalysts for the Oxygen Reduction Reaction. *Angew. Chem., Int. Ed.* **2019**, *58* (41), 14724–14730.
22. Han, A.; Wang, X.; Tang, K.; Zhang, Z.; Ye, C.; Kong, K.; Hu, H.; Zheng, L.; Jiang, P.; Zhao, C.; Zhang, Q.; Wang, D.; Li, Y. An Adjacent Atomic Platinum Site Enables Single-Atom Iron with High Oxygen Reduction Reaction Performance. *Angew. Chem., Int. Ed.* **2021**, *60* (35), 19262–19271.
23. Choudhary, K.; DeCost, B.; Chen, C.; Jain, A.; Tavazza, F.; Cohn, R.; Park, C. W.; Choudhary, A.; Agrawal, A.; Billinge, S. J. L.; Holm, E.; Ong, S. P.; Wolverton, C. Recent Advances and Applications of Deep Learning Methods in Materials Science. *Npj Comput. Mater.* **2022**, *8* (1).
24. Xu, P.; Ji, X.; Li, M.; Lu, W. Small Data Machine Learning in Materials Science. *Npj Comput. Mater.* **2023**, *9* (1).
25. Wang, S.; Jiang, J. Interpretable Catalysis Models Using Machine Learning with Spectroscopic Descriptors. *ACS Catal.* **2023**, *13* (11), 7428–7436.
26. Zhang, X.; Liu, J.; Li, R.; Jian, X.; Gao, X.; Lu, Z.; Yue, X. Machine Learning Screening of High-Performance Single-Atom Electrocatalysts for Two-Electron Oxygen Reduction Reaction. *J. Colloid Interface Sci.* **2023**, *645*, 956–963.
27. Ghanekar, P. G.; Deshpande, S.; Greeley, J. Adsorbate Chemical Environment-Based Machine Learning Framework for Heterogeneous Catalysis. *Nat. Commun.* **2022**, *13* (1).
28. Xie, X.; Peng, L.; Yang, H.; Waterhouse, G. I. N.; Shang, L.; Zhang, T. MIL-101-Derived Mesoporous Carbon Supporting Highly Exposed Fe Single-Atom Sites as Efficient Oxygen Reduction Reaction Catalysts. *Adv. Mater.* **2021**, *33* (23), 2101038.
29. Shang, H.; Zhou, X.; Dong, J.; Li, A.; Zhao, X.; Liu, Q.; Lin, Y.; Pei, J.; Li, Z.; Jiang, Z.; Zhou, D.; Zheng, L.; Wang, Y.; Zhou, J.; Yang, Z.; Cao, R.; Sarangi, R.; Sun, T.; Yang, X.; Zheng, X. Engineering Unsymmetrically Coordinated Cu-S1N3 Single Atom Sites with Enhanced Oxygen Reduction Activity. *Nat. Commun.* **2020**, *11* (1).
30. Xiao, M.; Zhu, J.; Li, G.; Li, N.; Li, S.; Cano, Z. P.; Ma, L.; Cui, P.; Xu, P.; Jiang, G.; Jin, H.; Wang, S.; Wu, T.; Lu, J.; Yu, A.; Su, D.; Chen, Z. A Single-Atom Iridium

- Heterogeneous Catalyst in Oxygen Reduction Reaction. *Angew. Chem., Int. Ed.* **2019**, *58* (28), 9640–9645.
31. Jeong, H.; Shin, D.; Kim, B.; Bae, J.; Shin, S.; Choe, C.; Han, J. W.; Lee, H. Controlling the Oxidation State of Pt Single Atoms for Maximizing Catalytic Activity. *Angew. Chem.* **2020**, *132* (46), 20872–20877.
  32. Nørskov, J. K.; Rossmeisl, J.; Logadottir, A.; Lindqvist, L.; Kitchin, J. R.; Bligaard, T.; Jónsson, H. Origin of the Overpotential for Oxygen Reduction at a Fuel-Cell Cathode. *J. Phys. Chem. B* **2004**, *108* (46), 17886–17892.
  33. Kresse, G.; Furthmüller, J. Efficient Iterative Schemes For a Total-Energy Calculations Using a Plane-Wave Basis Set. *Phys. Rev. B* **1996**, *54* (16), 11169–11186.
  34. Perdew, J. P.; Burke, K.; Ernzerhof, M. Generalized Gradient Approximation Made Simple. *Phys. Rev. Lett.* **1996**, *77* (18), 3865–3868.
  35. Blöchl, P. E. Projector Augmented-Wave Method. *Phys. Rev. B* **1994**, *50* (24), 17953–17979.
  36. Himmetoglu, B.; Floris, A.; de Gironcoli, S.; Cococcioni, M. Hubbard-Corrected DFT Energy Functionals: The LDA+U Description of Correlated Systems. *Int. J. Quantum Chem.* **2013**, *114* (1), 14–49.
  37. Xu, H.; Cheng, D.; Cao, D.; Zeng, X. C. A Universal Principle for a Rational Design of Single-Atom Electrocatalysts. *Nat. Catal* **2018**, *1* (5), 339–348.
  38. Chen, Y.; Ji, S.; Wang, Y.; Dong, J.; Chen, W.; Li, Z.; Shen, R.; Zheng, L.; Zhuang, Z.; Wang, D.; Li, Y. Isolated Single Iron Atoms Anchored on N-Doped Porous Carbon as an Efficient Electrocatalyst for the Oxygen Reduction Reaction. *Angew. Chem., Int. Ed.* **2017**, *56* (24), 6937–6941.
  39. Li, Q.; Luo, L.; Xu, C.; Song, S.; Wang, Y.; Zhang, L.; Tang, Y.; Texter, J. Palladium Enhanced Iron Active Site – an Efficient Dual-Atom Catalyst for Oxygen Electoreduction. *Small* **2023**.
  40. Medford, A. J.; Vojvodic, A.; Hummelshøj, J. S.; Voss, J.; Abild-Pedersen, F.; Studt, F.; Bligaard, T.; Nilsson, A.; Nørskov, J. K. From the Sabatier Principle to a Predictive Theory of Transition-Metal Heterogeneous Catalysis. *J. Catal.* **2015**, *328*, 36–42.



41. Yang, L.; Zhang, Y.; Huang, Y.; Deng, L.; Luo, Q.; Li, X.; Jiang, J. Promoting Oxygen Reduction Reaction on Carbon-Based Materials by Selective Hydrogen Bonding. *Chem. Eur.* **2023**.
42. Mitchell, S.; Pérez-Ramírez, J. Single Atom Catalysis: A Decade of Stunning Progress and the Promise for a Bright Future. *Nat. Commun.* **2020**, *11* (1), 4302.
43. Li, B.; Xie, H.; Yang, C.; Shi, C.; He, C.; Zhao, N.; Liu, E. Unraveling the Mechanism of Ligands Regulating Electronic Structure of MN<sub>4</sub> Sites with Optimized ORR Catalytic Performance. *Appl. Surf. Sci.* **2022**, *595*, 153526.
44. Rosen, A. S.; Notestein, J. M.; Snurr, R. Q. Structure–Activity Relationships That Identify Metal–Organic Framework Catalysts for Methane Activation. *ACS Catal.* **2019**, *9* (4), 3576–3587.
45. Ouyang, R.; Curtarolo, S.; Ahmetcik, E.; Scheffler, M.; Ghiringhelli, L. M. SISSO: A Compressed-Sensing Method for Identifying the Best Low-Dimensional Descriptor in an Immensity of Offered Candidates. *Phys. Rev. Mater.* **2018**, *2* (8).
46. Geurts, P.; Ernst, D.; Wehenkel, L. Extremely Randomized Trees. *Mach. Learn.* **2006**, *63* (1), 3–42.

## Associated Content

### Supporting Information

Computational details; schematic illustration of structural model construction and DFT workflow; free energy diagrams of 144 investigated SACs; DFT-computed data on catalytic properties of 144 SACs; plot of the relationships between  $\Delta G_{\text{OOH}^*}$  vs  $\Delta G_{\text{OH}^*}$  and  $\Delta G_{\text{OH}^*}$  vs  $\Delta G_{\text{O}^*}$  for 144 SACs;  $\Delta G_{\text{OH}^*}$  and  $\Delta G_{\text{O}^*}$  volcano plots for 144 SACs;  $\Delta G_{\text{OOH}^*}$  and  $\Delta G_{\text{O}^*}$  heat maps for 144 SACs; Correlation between group number of  $M_2$  and  $\Delta G_{\text{OOH}^*}$  for Fe-M system; Correlation between group number of  $M_2$  and overpotential for Fe-M system; Evaluation of prediction performance of electronic descriptor  $\psi$ ; Performance of SISO model using binding energies ( $\Delta G_{\text{OOH}^*}$ ,  $\Delta G_{\text{O}^*}$ , and  $\Delta G_{\text{OH}^*}$ ) to predict overpotential.

### Acknowledgment

The numerical calculations have been carried out on the supercomputing system provided by Beijing Paratera Co., Ltd. We thank Prof. Li Yang at Anhui University for her valuable methodological and software support.

Filename: Main\_text.docx  
Directory: C:\Users\82375\MyGoogleDrive\Qiuchengtong\manuscript\JPC  
L\ChemRxiv  
Template: C:\Users\82375\AppData\Roaming\Microsoft\Templates\Norma  
l.dotm  
Title:  
Subject:  
Author: Xijun Wang  
Keywords:  
Comments:  
Creation Date: 2023/8/8 12:12:00  
Change Number: 142  
Last Saved On: 2023/8/10 0:04:00  
Last Saved By: Xijun Wang  
Total Editing Time: 159 Minutes  
Last Printed On: 2023/8/10 0:10:00  
As of Last Complete Printing  
Number of Pages: 26  
Number of Words: 7,931 (approx.)  
Number of Characters: 45,213 (approx.)